Numerical modeling of residual type B aortic dissection: longitudinal analysis of favorable and unfavorable evolution

Khannous Fatma, Guivier-Curien Carine, Gaudry Marine, Piquet Philippe, Valerie Deplano

Numerical modeling of residual type B aortic dissection: longitudinal analysis of favorable and unfavorable evolution

Khannous Fatma[1] · Guivier-Curien Carine[1] · Gaudry Marine[1,2] · Piquet Philippe[2] · Deplano Valerie*[1]

[1] Aix Marseille Univ, CNRS, IRPHE-UMR7342, Ecole Centrale, Marseille, France

[2] Aix Marseille Univ, APHM, Timone Hospital, Department of Vascular Surgery, Marseille, France

*Corresponding author : valerie.deplano@univ-amu.fr

Abstract

Residual type B aortic dissection was numerically investigated to highlight the contribution of biomechanical parameters to the pathology's evolution. Patient-specific geometries from cases involving both favorable and unfavorable evolution were modeled to assess their hemodynamic features. This original approach was supported by a longitudinal study confirming the association between morphological changes, hemodynamic features, adverse clinical outcomes, and CT-angioscan observations on the same patient. Comparing one patient with unfavorable evolution with one with favorable one, we identify potential biomechanical indicators predictive of unfavorable evolution: (i) a patent false lumen with a flow rate above 50% of inlet flow rate; (ii) high wall shear stress above 18 Pa at entry tears, and above 10 Pa at some regions of the false lumen wall; (iii) low time-averaged wall shear stress in distal false lumen below 0.5 Pa; (iv) vortical structure dynamics. Although these comparisons could only be conducted on 2 patients and need to be confirmed by a larger number of cases, our findings point to these hemodynamic markers as possible candidates for early evaluation of the pathology's evolution towards an unfavorable scenario.

Keywords Residual type B aortic dissection · CFD simulations · Longitudinal study · Hemodynamical markers

1 Introduction

Aortic dissection is a cardiovascular pathology resulting in the disruption of the intimal layer of the aortic wall. As the tear extends, a false lumen adjacent to the arterial lumen is created, into which blood flows. True and false lumens are separated by a part of the dissected wall called the neointimal flap. Aortic dissections are commonly divided into type A (TAAD), which involves the ascending aorta, and type B (TBAD), which does not. While in the majority of TAAD cases (70%, [19]), the dissection reaches the descending aorta, initial surgical treatment replaces the ascending segment alone with a prosthesis. The remaining dissection is considered a residual type B aortic dissection (RTBAD) and is treated, like uncomplicated TBADs, by anti-hypertensive medical therapy, generally with good immediate results. In the long term, however, clinical data show that 28 to 36% of cases develop complications such as evolving aneurysm, ischemia, or aortic wall rupture [21]. Clinical studies have attempted to assess criteria that could be used to monitor RTBAD evolution. Statistical analysis suggested risk factors for adverse clinical events: degree of permeability of the false lumen [21, 25], development of partial thrombosis [40, 41], initial diameter of ascending aorta [44], and youth of patients [23]. Nevertheless, early prediction of RTBAD unfavorable evolution using these criteria remains challenging. Numerical simulations of aortic dissections have also been proposed, chiefly to link flow behavior with unfavorable evolution through hemodynamic indexes. Examples include wall shear stress spatio-temporal distribution and its derivative index [1, 18, 39], secondary flow dynamics [3, 33, 42], pressure and flow rate distribution [10, 13, 14]. A few of the most recent investigations considered fluid structure interaction (FSI) modeling ([5, 7] for example). However, these numerical studies rarely investigate RTBAD. Xu et al. [43] studied unfavorable aneurysm evolution only; Cheng et al. [13] used non-physiological outlet boundary conditions; Chen et al. [12] focused on drug treatment effects on hemodynamics; Baumler et al. [7] pointed out the importance of taking into account flap mobility. To our knowledge, no study examined RTBAD patient-specific geometries representative of both favorable and unfavorable evolutions, with their associated follow-up times. Menichini et al. [33] actually studied CT scans

of the first follow-up to determine whether or not there was thrombus formation, but did not perform numerical simulations at that follow-up time.

The main goal of the present numerical simulations is to investigate hemodynamics and propose to correlate description of flows, quantification of hemodynamic parameters and vortical structures, with clinical events observed during postoperative follow-ups in the context of RTBAD, for early identification of biomechanical factors predictive of the pathology's evolution. Investigating both favorable and unfavorable evolutions at two different post-operative time permits a comparative analysis of hemodynamics in different anatomical topologies. For each case, we are able to describe and characterize velocity fields, flow rate distributions inside both lumens, vortical structures'dynamics, and spatio-temporal wall shear stress distributions up to correlate them with clinical events. It is important to note that, to our knowledge no longitudinal study on RTBAD provides a description and quantification of vortex structures and correlates them with actual clinical observation of thrombus formation.

2 Materials and methods

2.1 Geometries

Two patients with RTBAD after surgical repair of type A aortic dissection were considered at two different times during their CT-angioscan follow-up. Both patients gave their informed consent and none of them have any congenital or genetic diseases. One, a patient with favorable evolution called "favorable case" (FC), was a 58-year-old male. The other, a patient with unfavorable evolution called "unfavorable case" (UFC), was a 68-year-old male. The criterion used to discriminate UFC from FC was the necessity of an endovascular intervention within 5 years after a first surgical implantation of a Dacron prosthesis on the ascending aorta. UFC required endovascular intervention 27 months after the prosthesis implantation due to aneurysmal evolution. On the contrary FC didn't require intervention at least 5 years after his prosthesis implantation. Two geometrical models were developed for each patient. T_0 refers to the CT-angioscan performed just after surgical repair of type A aortic dissection using a prosthesis. T_1 refers to the angioscan performed one year later ($T_1=T_0+12$ months). CT-angioscans were performed at Timone Hospital, Marseille using a Siemens apparatus (sensation 64). The CT-angioscan images, were grouped in a set of 2D 1 mm thickness slices with a size of 512×512 pixels and a plane resolution lower than of 0.89 mm/px, encoded in 16-bit grayscale. The interslice distance is about 1 mm. The 3D reconstruction of the aorta was then performed using image-processing software Invesalius 3.1 (CTI, Brazil). The regions of interest (true and false lumens) were captured by applying to each CT-slice the watershed segmentation method [30], which is based on the grayscale intensity of the images. The marching cubes algorithm [29] was then applied automatically on the stacked and segmented slices to form the 3D surface with triangular grids. Once reconstructed, the geometries were exported into Ansys SpaceClaim package (Ansys, Inc.) and smoothed to eliminate any reconstruction errors. The volume difference between initial reconstruction and smoothed one did not exceed 2%. The ascending segments of the aorta were modeled into cylinders since they were covered by prostheses of constant diameter. Their inlet diameters, D, directly measured on the CTA by clinician, were equal to 4.0 cm and 3.4 cm for UFC and FC respectively. The two main diameters of the entry and re-entry tears were assessed with CTA on each patient. In agreement with the clinicians elliptical shapes were chosen to reflect their contours.

Each geometry included the ascending aorta (prosthesis), the aortic arch and its 3 branches (BCA: brachio-cephalic artery; outlet S_1, LCCA: left common carotid artery; outlet S_2 and LSA: left subclavian artery; outlet S_3), the descending aorta (DA; outlet S_4) that stops at the celiac trunk (CeT) and the flap separating true lumen (TL) from false lumen (FL) whose patent parts were reconstructed. Thrombus was not included. The distal end of UFC dissection was located at CeT and ended by a tear making true and false lumens confluent, as it was previously observed and modeled by [13, 33, 43]. For FC, CT-angioscan images were not available after CeT. Aware that geometrical conditions can change the results obtained, we decided to end the FC dissection at CeT, as UFC, to compare both cases. Consequently, as the first main collateral branch of the descending aorta is the CeT no collateral branches were included except the 3 aortic branches from the aortic arch. The geometries of both cases and follow-ups are shown in Fig. 1a, b, e, f.

2.2 Numerical simulations

The 3D time-dependent incompressible Navier-Stokes equations that governed the blood flow were solved using a finite-volume method implemented in Ansys Fluent software (Ansys Inc., 19.1 version). A pressure velocity coupling method (coupled method in Fluent) was chosen and second order schemes for both spatial and temporal discretization were used. Five periods were simulated to ensure periodicity and the results obtained during the last period were used for post-processing since velocity and pressure results differed by less than 1% on average for several spatial planes of interest between the 4th and the 5th period. One cycle was divided into time steps of 10^{-3}s. A root mean square residual less than 10^{-4} was used to ensure the convergence of the solution. This value was validated by prior benchmark tests [27].

The average Reynolds, $Re_{mean} = \frac{\rho U_{mean} D}{\mu_\infty}$, with μ_∞ =0.0035 Pa s the dynamic viscosity, $\rho = 1060$ kg m^{-3} the density and, U_{mean} the inlet mean velocity, was 1504.9 and 1279.2 for FC and UFC case respectively. The maximum Reynolds number, $Re_{max} = \frac{\rho U_{max} L}{\mu_\infty}$, was 3116 and 4785 for FC and UFC case respectively. They were obtained using the maximum axis of the ellipsoidal tear shape for L and the maximum velocity, U_{max}, found at entry tears during systolic peak. The Womersley number, $\alpha = R\sqrt{\frac{\rho \omega}{\mu_\infty}}$ with ω =2π/T, was 23.4 and 27.6 for FC and UFC case respectively.
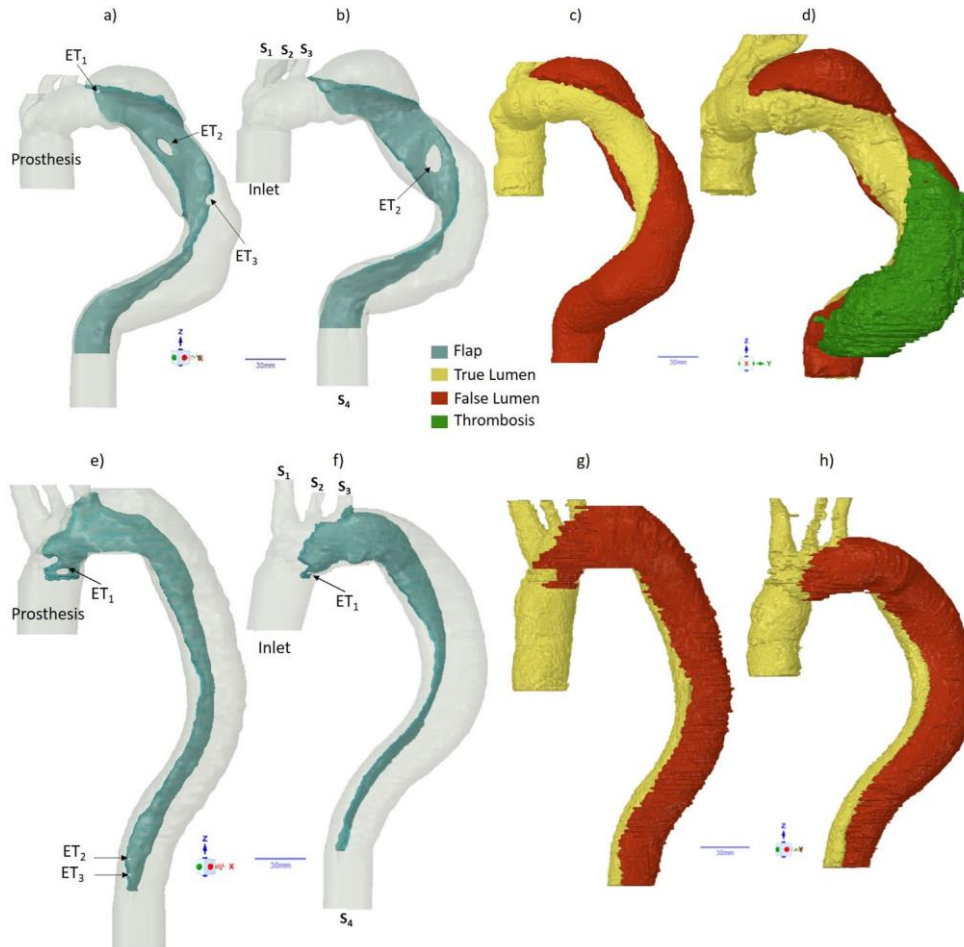
Fig. 1 Scheme and clinical observations of unfavorable case (UFC):first line; favorable case (FC): second line. For both follow-ups T0: (a), (c), (e), and (g); T1: (b), (d), (f), and (h). ET1, ET2, and ET3: entry tear numbers 1, 2 and 3 respectively. (c), (d), (g) and (h) are the raw CT-angioscan segmentation that stops at CeT. (a), (b), (e) and (f) are the geometrical models used for the simulations after smoothing and with the addition of an outlet tube

These values were the same for T_0 and T_1 models. The minimum critical Reynolds number values [2], equal to 5850 and 6900 for FC and UFC respectively were higher than the Re_{max} in both cases. Blood flow was thus assumed to be laminar. Blood was modeled as a nonNewtonian incompressible fluid with a dynamic viscosity given by the Carreau-Yasuda model [9] and [28].

$$\frac{\mu - \mu_\infty}{\mu_0 - \mu_\infty} = [1 + (\lambda \dot{\gamma})^a]^{(n-1)/a}$$

with $\mu_0 = 0.16$ Pa s, $\lambda = 8.2$s, n=0.2128 and a=0.64.

2.2.1 Meshes

Volume meshes were created with Ansys Fluent meshing 19.1. For each geometry, a hybrid grid was generated, combining tetrahedrons in the core region and 5 prismatic cell-layers near the wall to account for the unsteady boundary layer. The latter's thickness, δ, of 0.725 mm was determined according to Fung's definition [22] as inversely proportional to the Womersley number, α, $\delta = \frac{R}{\alpha}$, R being the radius of the aorta. Maximum element length was 1.5 mm and the first prismatic layer was 0.1 mm thick. Mesh sensitivity of the results was performed on velocity field obtained at entry tears and on time-averaged wall shear stress (TAWSS) values. For example for UFC, the most tortuous geometry, at T_0, three meshes were considered of about 5, 1.8 and 1.2 millions mixed elements named M1, M2 and M3 respectively. For the velocity fields and TAWSS values the relative difference were of 5%, 8% and of 5%, 20% between M1 and M2 and M1 and M3 respectively. For one cardiac period, the computational time was 2.5 and 3.4 times lower for M2 and M3 respectively. Examining the mesh sensitivity of the results obtained and considering the computational time gave the final mesh of UFC as a total of 1,832,285 (M2 mesh) and 2,326,577 mixed elements for the T_0 and T_1 models respectively, and the final mesh of FC was 1,737,504 and 2,033,642 mixed elements respectively for the two models.

2.2.2 Boundary conditions

The inlet velocity profiles were calculated from the flow rate of the ascending aorta given in [35] as the analytical Womersley solution of a fully developed periodic flow in a cylindrical tube. The same flow rate was used for both UFC and FC, with velocity magnitudes depending on the inlet diameter of each case. The same velocity profile was used for both T_0 and T_1 models.

A time-dependent periodical pressure profile was applied at each outlet, S_1, S_2, S_3, and S_4 (Fig. 1), modeling the hypotensive therapy prescribed by surgeons to the patients with dissection. These physiological pressure values were obtained using 3-element Windkessel models (R_1,R_2,C) with R_1 the proximal resistance, R_2 the distal one, and C the capacitance. For each case and follow-up, the model parameters (R_1,R_2,C) for each outlet were identified through an optimization procedure using a genetic algorithm on Matlab software. The optimization consisted in finding R_1^i, R_2^i, and C^i for each outlet i that minimize the mismatch between the computed and the targeted pressure values corresponding to the hypotensive therapy. For more details of Windkessel model implementation and generated flow rate distribution at outlets, see Appendix.

Prosthesis, aortic walls and flap were assumed to be rigid, with no slip boundary conditions.

3 Results

3.1 Morphological changes

Morphological differences between UFC and FC and changes between T_0 and T_1 for each case were first determined using 3D geometrical reconstructions and clinical observations through CT-angioscans (Fig. 1).

T_0 UFC initial ascending aorta diameter was 15% larger than that of FC. At T_0, there were 3 entry tears (ET) in each case. For UFC, ET were located downstream of the S_3 outlet, while for FC, the first ET was at the beginning of the aortic arch and the two others were in the descending aorta lower segment, near the S_4 outlet (Fig. 1). ET dimensions differed between cases and followups (Table 1): those of UFC were larger. For UFC, at T_0, the ET_1, ET_2, and ET_3 areas were 4.34, 38.5 and 35.9 times larger than those of FC respectively. At T_1, the UFC ET_1 area reached 12.69 times that of FC. Moreover, while the FC ET_1 area decreased by 41%, between T_0 and T_1, that of UFC increased by 72.1%. In addition, FC ET_2 was no longer

detectable, whereas UFC ET_2 increased by 58.7%. In both cases, ET_3 disappeared. For FC, it could not be observed under the scanner resolution, while for UFC, it was obstructed by the partial thrombosis of the distal FL (Fig. 1d).

An overall expansion of true and false lumen volumes was observed between T_0 and T_1. The lumen volumes correspond to their patent segments. The UFC false lumen increased more than that of FC (26.9% versus 19.4%), whereas the UFC true lumen increased less than that of FC (5.9% versus 8.4%). For UFC, the major dilation was observed downstream of the LSA. These expansions were linked to an increase of 15.7% and 6.3% in total aorta diameter for UFC and FC respectively. It is important to note that, despite a lack of re-intervention for the FC 5 years after T_0, aortic remodeling was observed at T_1 for both cases. Morphological characteristics and changes, as well as ET spatial locations, will impact flow patterns and flow rate distribution.

3.2 Flow behavior

The geometry of the dissected aorta is characterized by a tortuous shape with curvatures and narrowings and widenings of sections creating a complex flow. The aortic arch, the main curvature of the aorta, or aortic plications induce changes in fluid

	FC			UFC		
	ET_1	ET_2	ET_3	ET_1	ET_2	ET_3
Area at T_0, (A_{T_0}), in (cm^2)	0.90	0.11	0.11	3.91	4.24	3.95
Area at T_1, (A_{T_1}), in (cm^2)	0.53	NA	NA	6.73	6.73	NA
$\frac{A_{T_1}-A_{T_0}}{A_{T_0}}(\%)$	-41.1	NA	NA	72.1	58.7	NA

	FC		UFC	
	V_{FL}	V_{TL}	V_{FL}	V_{TL}
Volume at T_0, (V_{T_0}), in (cm^3)	166.8	151.3	273.2	208.1
Volume at T_1, (V_{T_1}), in (cm^3)	199.3	164.1	346.9	220.4
$\frac{V_{T_1}-V_{T_0}}{V_{T_0}}(\%)$	19.4	8.4	26.9	5.9

Table 1 Entry tear (ET_i) areas and True or False lumen volume (V_{TL} or V_{FL}) at T_0 and T_1 for UFC and FC.

direction leading to centrifugal forces. A combination of viscosity force, centrifugal force, and its opposite transverse pressure gradient then give rise to counter-rotating vortices, which develop in planes perpendicular to the principal flow and propagate helically. Furthermore, ETs induce section narrowing, creating jetlike flows. This highly accelerated flow enters the FL and can impact the opposite FL wall. Conversely, sudden widening of the section downstream of the ET leads to slow recirculation zones. Jet flow in the FL, associated with section widening, generates velocity discontinuity resulting in a rolling up shear layer (Kelvin-Helmholtz instability). This creates 3D vortical structures that propagate in the FL, as observed in abdominal aortic aneurysm [16].

Although these general features were observed for both cases and follow-ups, specific flow behavior patterns were noted.

Favorable versus unfavorable case Flow characteristics were analyzed at different times in the cardiac cycle and in different planes, including parallel plane to the main flow passing through ET_1 and ET_3 (Fig. 2) and perpendicular planes (Fig. 3).
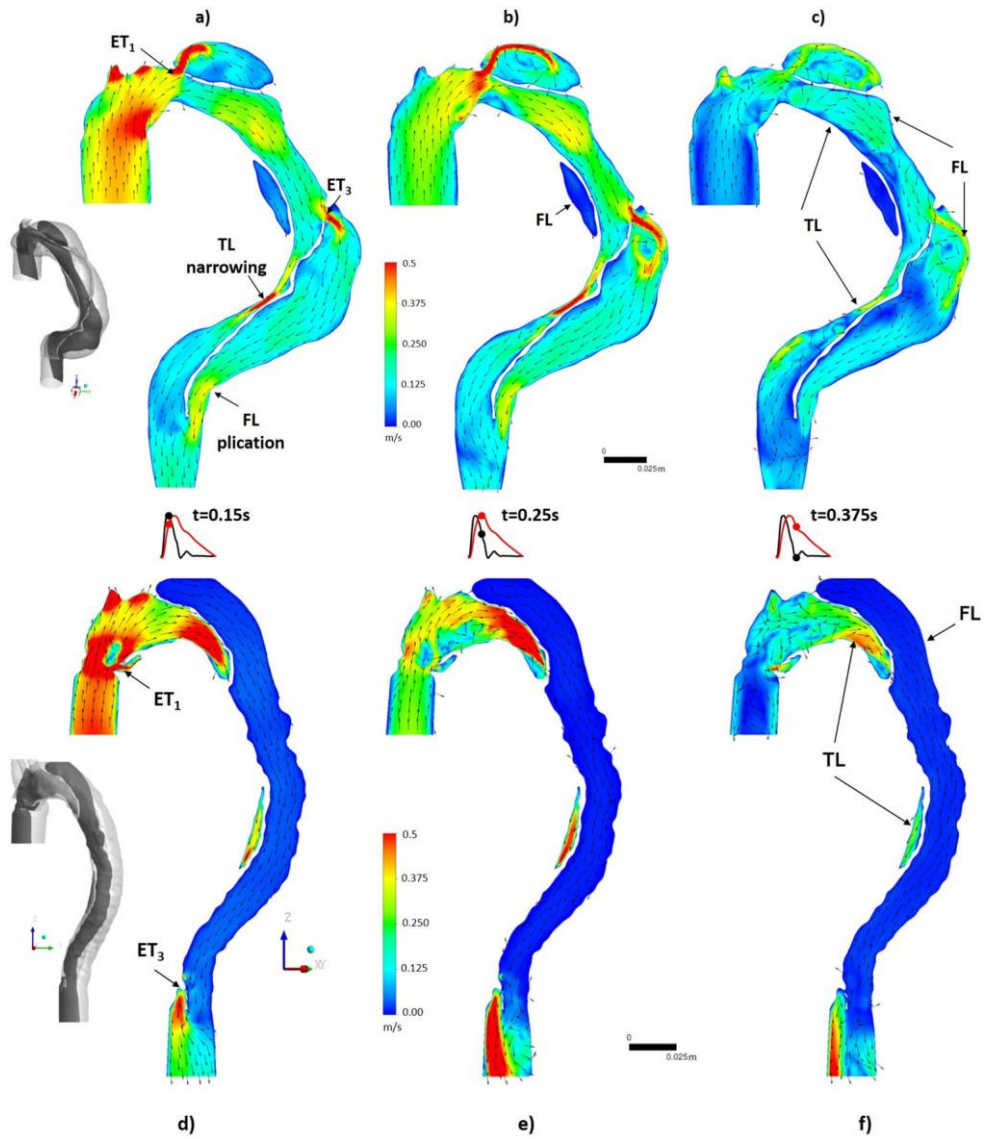
Fig. 2 Velocity vectors superimposed on velocity iso contours at T0 in planes parallel to main flow, see gray plane schemes, and at different times in cardiac cycle t = 0.15 s (a, d), t = 0.25 s (b, e), and t = 0.375 s (c, f). First line UFC (a, b, c). Second line FC (d, e, f). Pressure curves in red, flow rate ones in black. ET1 and ET3 are entry tear numbers 1 and 3 respectively. TL and FL are true and false lumen respectively
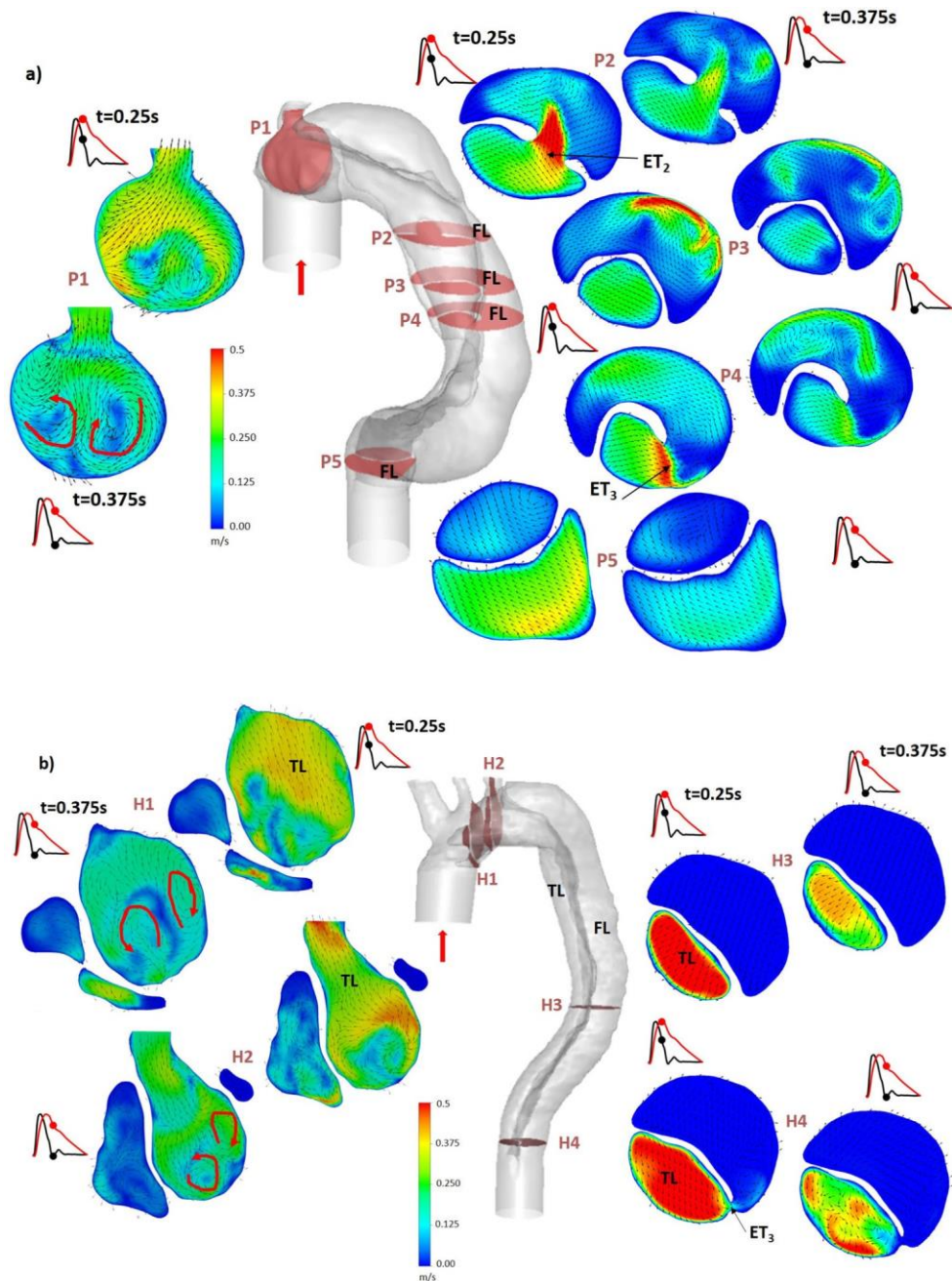
Fig. 3 Velocity vectors superimposed on velocity iso contours at T_0 in planes perpendicular to main flow, see red plane schemes, and at t = 0.25 s and t = 0.375 s. Pressure curves in red, flow rate ones in black. (a) UFC; (b) FC

At systolic peak, t = 0.15 s (Fig. 2a and d), jet flows were observed for both cases at ET, at TL narrowing, and to a lesser extent at UFC plication of the FL. Contrary to UFC, a strong velocity dissymmetry was observed between true and false lumen for FC, with very low velocity values in the FL (Figs. 2d–f and 3b H3 and H4 planes).

During the flow rate deceleration phase (t = 0.25 s), recirculating areas appeared at the aortic arch curvature for both cases (Fig. 2b and e, however the jet flows progressed downstream along the FL only for UFC (Fig. 2b). Very complex secondary structures were observed in the TL of the aortic arch for both cases (Figs. 3a P1 plane and 3b H1 and H2 planes); however, in the FL, they only appeared for UFC (Figs. 2b and 3a). Importantly, in the descending aorta at t = 0.375 s (Fig. 2c and f), the flow was upstream for FC and downstream for UFC. This inversion of the flow from the false to the true lumen,

particularly at ET_1, was also observed in H3 and H4 planes at t = 0.375 s (Fig. 3b) and continued until the end of the cardiac cycle.

The same phenomena were observed at T_1 for each case (not shown), with greater or lesser amplitude according to the morphological changes.

To quantitatively determine the major differences between the cases, the flow rate distribution was estimated over the cardiac cycle on specific planes downstream of the entry tears. A plane was, for example, placed downstream of ET_1 and upstream of ET_2. With this plane located downstream ET_1, at T_0, $\frac{\bar{Q}_{TL}}{Q_{FL}} =$ 2.77 and 45.82 for UFC and FC respectively; at T_1 these ratios were 1.88 and 77.31. It was also important to quantify the outlet FL flow rate in relation to the inlet flow rate. Considering a plane located after ET_3 when it exists and after ET_2 otherwise, at T_0, $\frac{\bar{Q}_{FL}}{Q_{inlet}} = 0.56$ and 0.0142 for UFC and FC respectively; at T_1 these ratios were 0.53 and 0.0071.

3.3 Vortical structures

3D vortical structures (VS) were identified using the λ_{ci} criterion which is based on the imaginary part of the complex conjugate eigenvalues of the velocity gradient tensor [45]. VS were found mainly in the FL for UFC (Fig. 4a–i) and in the TL for FC, where there were also a few weak structures in the FL that did not spread downstream (data not shown).

At T_0 in UFC, ring-shaped vortices (VR) were observed to have formed at the necks of the entry tears at the beginning of the cardiac cycle. At t = 0.075 s, the VR from ET_1 detached from its neck, while those from ET_2 and ET_3 detached later at t = 0.1 s (Fig. 4a and b). They were then convected downstream and, depending on FL dimensions and the incidence angle of the jet flow e.g the dimensions and locations of the entry tears, they impacted the FL external wall at different times in the cardiac cycle: at t = 0.15 s, 0.22 s and 0.26 s for VR from ET_1, ET_2 and ET_3 respectively (Fig. 4b and c for example). VR can have different forms and axes of rotation because of the patient geometry complexity: the VR from ET_1 and ET_3 lost their ring shape and flattened, unlike that from ET_2.

During the deceleration phase, VS convection was accompanied by subdivision into smaller structures, at t = 0.25 s for VS from ET_1 and at t = 0.3 s for those from ET_2 and ET_3 (Fig. 4d). Finally, at the end of the cycle, VS dislocated, while new structures were observed to have formed at the necks of the entry tears (Fig. 4e).

At T_1 in UFC, the same overall phenomena were observed. One difference was that larger structures formed downstream of ET_1, due to the bulge expansion there and to an increase of ET_1 surface area by roughly 72% compared to T_0 (Fig. 4g and Table 1). Moreover, VR from ET_1 had an earlier impact (Fig. 4f). The ET_2 surface area increase (58.7% compared to T_0) generated a change in the incidence angle of the jet flow (Fig. 4g and h) and modified both VR impact time (t = 0.27 s versus t = 0.22 s) and impact zone, shifting it downstream by about 50 mm. After the impact, the VS were subdivided into smaller structures than those observed in T_0 (Fig. 4). As ET_3 was obstructed by thrombosis, no further VS were observed in the FL downstream of this entry tear, unlike in T_0.

Later in this article (Section 3.6.2), we will discuss the link between the VR dynamics, the wall shear stress evolution (Section 3.4) and the clinical events
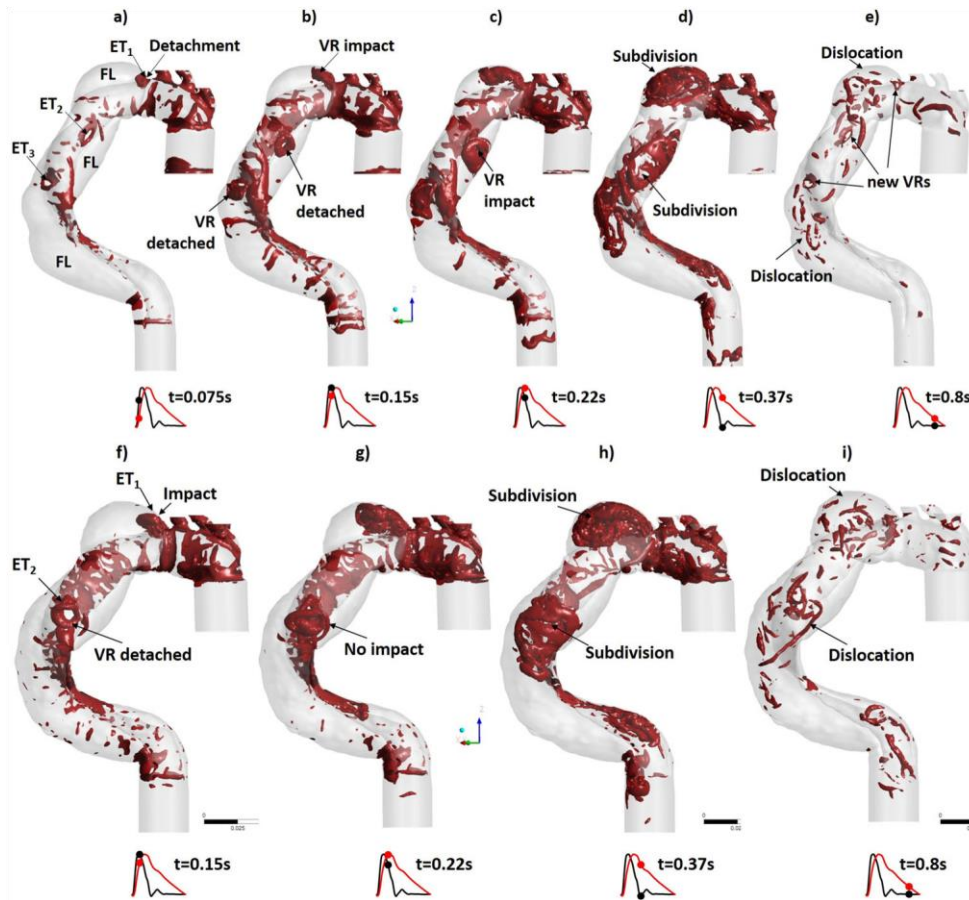
Fig. 4 :λci = 19.5 s−1 iso contours for UFC at different times in cardiac cycle t = 0.075 s (a), t = 0.15 s (b, f), t = 0.22 s (c, g), t = 0.37 s (d, h) and t = 0.8 s (e, i). First line T0 (a, b, c, d, e). Second line T1 (f, g, h, i). Pressure curves in red, flow rate ones in black. ET1, ET2 and ET3 are entry tear numbers 1, 2 and 3 respectively. FL is false lumen. VR is ring-shaped vortex

3.4 Wall shear stress and derived index

Amplitudes of wall shear stress (WSS), time-averaged WSS (TAWSS), and oscillatory shear index (OSI) were determined for both cases and follow-ups. According to the flow behavior, whatever the case and follow-up, high WSS values were observed at curvatures or plications, at narrowings, and at walls where VR impacted. In parallel, regions of very low WSS ($\leq$ 1 Pa) occurred at the distal FL.

Figure 5 illustrates most of the features related to high WSS for UFC and both follow-ups. At T_0, at systolic peak (t = 0.15 s), WSS reached 21.68, 20.41 and 18.23 Pa at ET_1, ET_2, and ET_3 respectively. These values increased by 37.68% for ET_1 at T_1. At both follow-ups, this high WSS level was maintained until mid-deceleration (t = 0.25 s). VR impact also induced high WSS on the FL walls facing entry tears: 14.58 Pa, 10.74 Pa, and 5.82 Pa at ET_1, ET_2, and ET_3 respectively at T_0. Between T_0 and T_1, the WSS value generated at VR impact for ET_1 increased by 22.15%, while that of ET_2 decreased by 13.5%.

TAWSS distribution (Fig. 6) highlighted the differences between UFC and FC concerning low WSS zones. At both UFC follow-ups, they were located downstream of ET_3 in the lower part of the FL, while they extended along the entire FL in FC. In the latter case, the low TAWSS region ($\leq$ 0.5 Pa) occupied 45.3% of the total aortic wall surface.

OSI distribution (Fig. 7) indicated that in both cases, entry tear areas and VR impact zones were subjected to low OSI, almost 0 for ET for example. Moreover, as mentioned by [37] or [5], high OSI values appeared mainly in areas where TAWSS values were low; for example, downstream and upstream of ET_3 of the UFC FL at T_0, or in the distal FL for both follow-ups of UFC. On the contrary, for FC, there was a strong discrepancy between TL and FL values. In the TL, OSI values were low; the flow was mainly in the axial direction. In the FL, OSI values were very high (≥ 0.4); the flow became upstream from t = 0.375 s up to the end of the cycle. The FL of FC was subjected to higher OSI values than that of UFC.
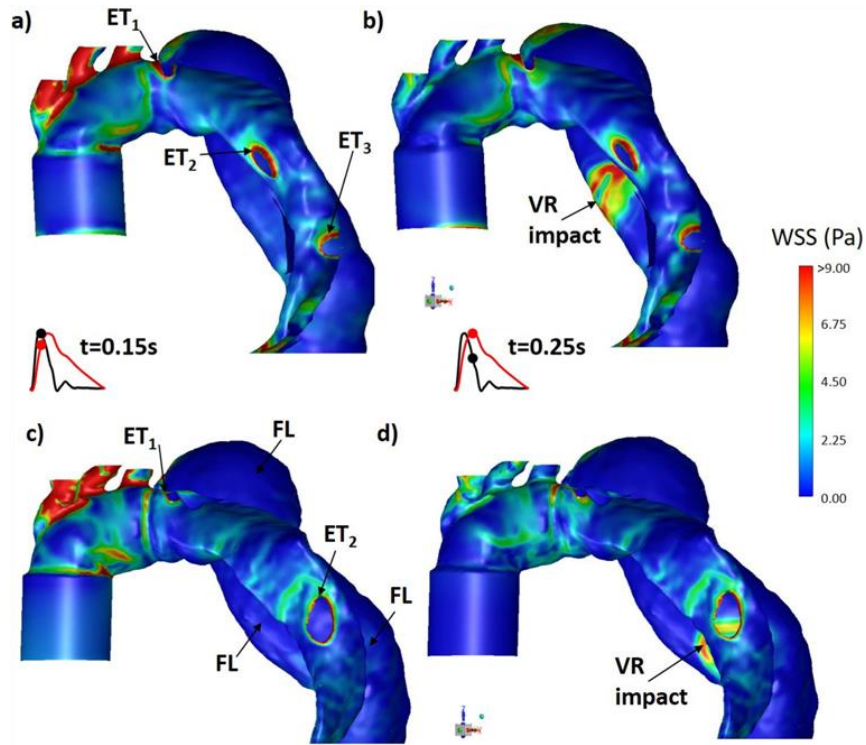

Fig 5 : Iso contours of WSS at t = 0.15 s and t = 0.25 s. Pressure curves in red, flow rate ones in black. (a) and (b) UFC, T0; (c) and (d) UFC, T1
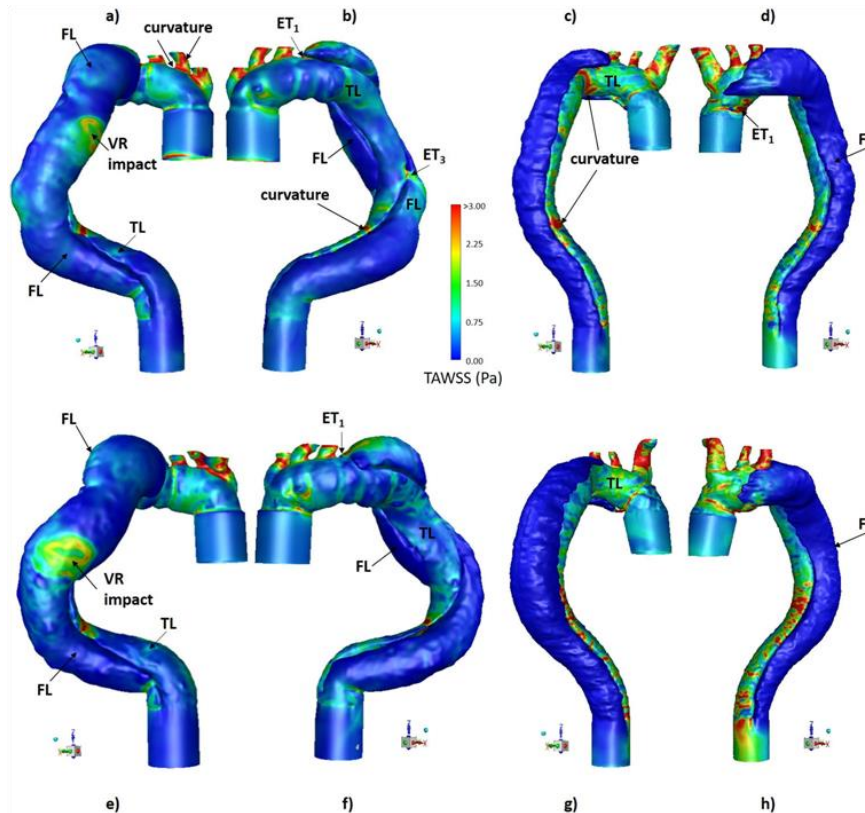
Fig 6: Iso contours of TAWSS. First line T0 for (a) and (b) UFC and (c) and (d) FC. Second line T1 for (e) and (f) UFC and (g) and (h) FC

3.5 Pressure distribution

Whatever the case and follow-up, up to t = 0.375 s, pressure values were higher in the upper part of the aorta than in the lower part; after that, the trend reversed (Fig. 8). These results are in agreement with previous studies [3, 4]. For UFC, values were higher in the TL than in the FL throughout almost the entire cardiac cycle, in accordance with the single direction of blood exchange between the two lumens revealed by the flow rate distribution. Moreover, pressure was mainly uniformly distributed along the FL wall, with the exception of jet-impingement areas, where a local increase in pressure reaching 120 mmHg was observed during the mid-deceleration phase (t = 0.25 s). Homogeneous pressure values between the two lumens were probably due to the outlet conditions, which reproduce the drug treatment effect. These results are consistent with [12], who demonstrated that drug treatment decreases pressure values in the aorta and homogenizes pressures, in particular in the FL. According to [4, 8, 37], ET also plays a role in pressure balancing between the two lumens, with pressure dropping during diastole. Finally, open endedness of the FL in both cases and rigid wall assumption can also contribute to homogeneous pressure values between the two lumens. For FC, two major discrepancies were observed. From t = 0.375 s, pressure in the FL became higher than in the TL, consistent with flow being directed from the FL to the TL; jet-impingement did not cause a local increase in pressure. For both cases, pressure distribution at T_1 (data not shown) was roughly equivalent to that at T_0.

3.6 Discussion

Few numerical studies of aortic dissection have performed longitudinal patient monitoring to analyze the evolution of the pathology. The present work applied this approach to study patients with favorable (FC) and unfavorable (UFC) evolution at 2 follow-ups each over 12 months. We chose to impose the same physiological inlet flow rate and outlet pressure curves when modeling these patients on antihypertensive drug treatment at the 2 follow-ups, to obtain a better understanding of the role of each biomechanical parameter in the pathology's evolution. Maintaining the same medical context allowed us to identify correlations between hemodynamics and the evolution of the patient. The results confirmed that geometrical

characteristics of the dissection morphologies: curvatures, localizations and sizes of entry and re-entry tears, dilations, dimensions of the lumens, impact flow dynamics and related hemodynamics quantities such as vorticity, wall shear stress and flow rate. Flow patterns differ not only between UFC and FC but also for a given case between follow-ups.
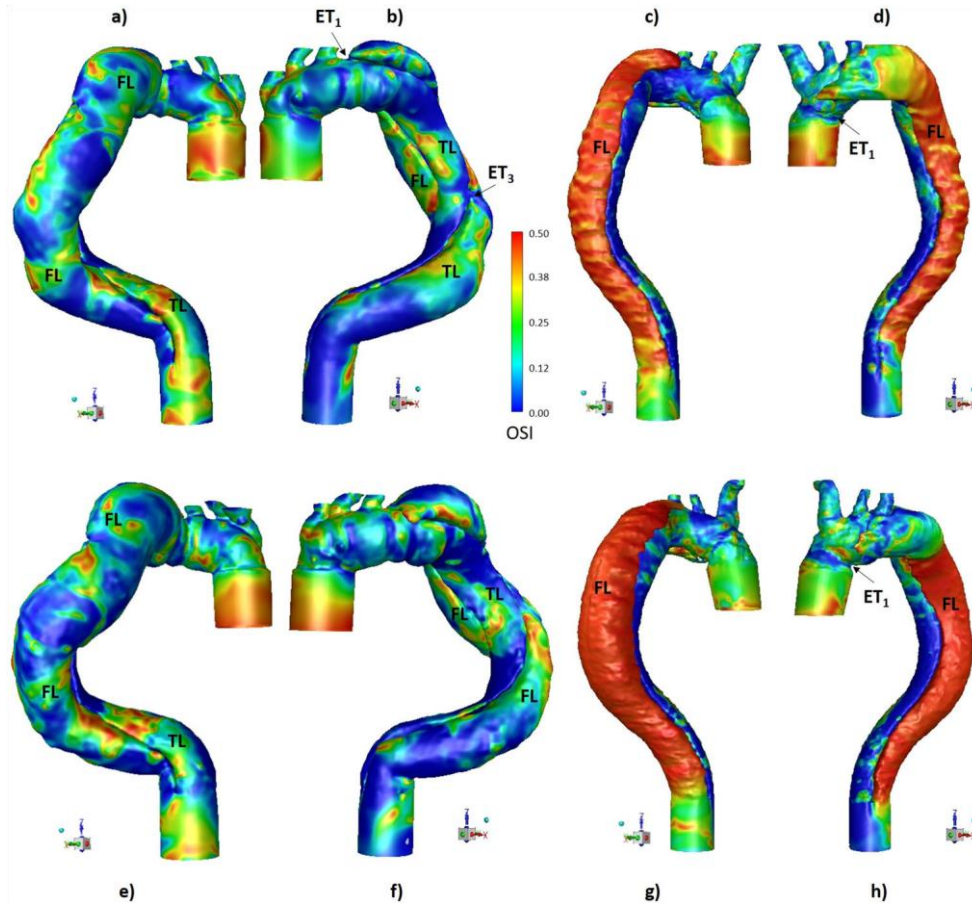

Fig. 7 Iso contours of OSI. First line T_0 for (a) and (b) UFC and (c) and (d) FC. Second line T_1 for (e) and (f) UFC and (g) and (h) FC

3.6.1 Flow rate, dilation

At both FC follow-ups, CFD results showed a flow rate that remained almost zero in the false lumen. FC CTangioscan analysis at T_1 indicated a favorable evolution for this patient. These outcomes are consistent with some clinical studies showing that a low flow rate in the false lumen is associated with absence of complications [25, 40]. Conversely, CFD performed at both UFC follow-ups revealed a patent false lumen with an average flow rate reaching 57% of the inlet flow rate. This was associated with an overall FL volume increase of 27% at T_1. These results are in agreement with clinical observations [20, 21, 44] linking the presence of a completely patent FL with faster growth in diameter (≥ 3 mm/year) which can evolve into aneurysm, like the dilation observed in the present work at T_1 for UFC, leading to a decision to reoperate. Some studies suggest that a combination of low WSS and high OSI is linked to an inflammatory response of the endothelium that leads to its degradation and notably promotes dilation, such as the development of aneurysm. In case of dissection, consisting in a separation of the aortic wall layers occurring mainly at the media [37], this process could be associated with endothelialization of the FL that could occur in chronic case [11]. Aortic diameter dilation, on the other hand, is found to be correlated to elevated WSS values [1, 24, 39]. In our case, high WSS values were observed on the FL wall facing the entry tears at jet impact zones. At T_1, the aortic diameter increased in relation to T_0 by 15.7% and 6.3% for UFC and FC respectively. This widening resulted in increased FL volume for both cases, with greater dilation in UFC evolution (27% vs

19%). Recent studies [15, 34] explained the formation of aneurysms through a mechanical model of the wall that took into consideration only the media and adventitia layers (i.e without endothelial cells). They highlighted the aortic wall's sensitivity to variation in forces, including pressure, and the influence of these variations on homeostatic equilibrium. In pathological situations, the internal stress state of the wall may no longer enable it to counteract pressure forces, due to dysfunctional degradation and production of the components of the wall (elastin, collagen, etc.), causing loss of integrity and irreversible dilation. Mousavi et al.
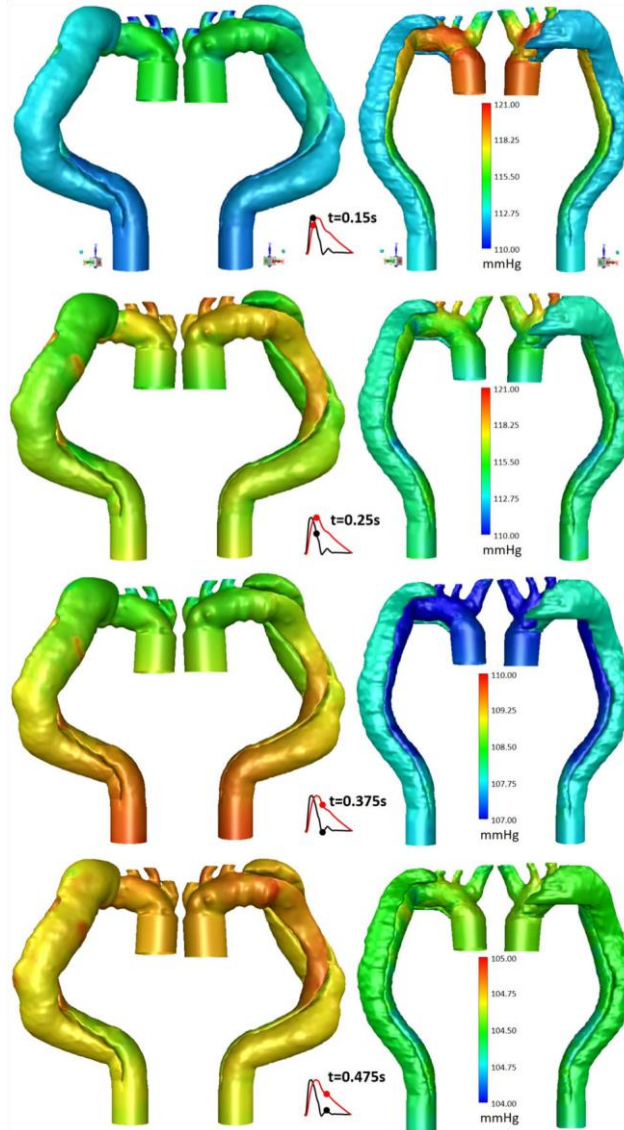

Fig. 8 Iso contours of pressure at T_0 for t = 0.15 s, 0.25 s, 0.375 s and 0.475 s. Pressure curves in red, flow rate ones in black. First row: UFC. Second row: FC

[34] linked wall expansion to elastin degradation, and this process was associated by [24] with high WSS values.

In the present study, damage to the FL wall during dissection could have triggered a process of elastin degradation. Both jet flow and VS impact on the FL wall help create high WSS zones. Repeated increases in local pressure on the FL outer wall, combined with jet impingement, may also cause a progressive enlargement of FL diameter over time. This combination could thus explain the FL expansion observed, particularly in UFC. In FC, the wall was less exposed to the impacts of the jet flow and VS, which would explain the lower FL expansion observed at T_1 relative to that of UFC.

3.6.2 Thrombus formation

According to [26], the platelet activation threshold is ~ 10 Pa, activation requires an estimated exposure time of ~ 100 ms, and a stress level of about 18 Pa can induce platelet aggregation. Studies on platelet activation and thrombosis [31, 32, 38] have demonstrated that adhesion of activated aggregated platelets to the wall occurs when WSS/TAWSS values are low ($<$ 0.5 Pa [3]), subsequently initiating thrombus formation. At the same time, clinical observations have correlated partial thrombus formation in the FL with deleterious clinical events and the risk of patient re-operation [40, 41]. We found high WSS values at entry tears, exceeding 20 Pa during systole in both cases. Moreover, VS analysis in UFC showed that several vortices form at the entry tear necks from the beginning of the cardiac cycle. During the systolic phase, these vortices detach from the neck and are convected downstream to the FL lower segment. At the end of the cardiac cycle, the VS break up near the wall. Their dislocation is located between 40 and 50 mm (Fig. 4e) downstream of the ET_3, where low TAWSS values (Fig. 6) were observed.

As described by [3], the role of vortical structures is thus manifold: (i) they trap the platelets which are, for the most part, activated because of the high WSS encountered at the entry tears; (ii) they promote spontaneous platelet aggregation through rotational fluid motions which cause prolonged collision of activated platelets in a high-shear environment; (iii) they convect the activated/aggregated platelets downstream, iv) they release them during their dislocation or impact near a wall where low WSS is observed. The combined role of VS dynamics and WSS, highlighted at T_0 for UFC, in thrombus formation is confirmed here for the first time, thanks to our clinical observations of UFC evolution at T_1. Non existent at T_0, thrombosis in the lower part of the FL, localized where T_0 CFD predicted VS dislocation and low TAWSS values, is clearly visible in CT-angioscan at T_1 (Fig. 1d). This thrombus developed, reaching and obstructing the ET_3.

In contrast, FC analysis shows that few vortices formed in the FL. This confirms that VS formation per unit of volume is partly proportional to FL diameter ($D_{UFC} = 29.4$ mm, $D_{FC} = 17.4$ mm) [3]. In addition, an upstream flow appeared at the end of the systole, which may explain the absence of activated platelets convected towards the FL lower region. Together, these two phenomena likely prevented thrombus formation in distal false lumen of FC, a hypothesis that was confirmed by clinical observations at T_1 (Fig. 1h).

VS dynamics has been little studied in the context of aortic dissections. The present comparative analysis conducted between UFC and FC at two follow-ups confirms that VS development in the FL negatively impacts the pathology's evolution. It should be noted that areas prone to concomitant low TAWSS and high OSI in the false lumen of FC are not associated with adverse clinical events in the absence of vortical structure development.

3.6.3 Limitations

One limitation of this work is related to the number of patients. With one case per outcome (FC versus UFC) this study will have to be extended to more patients to confirm our results. Moreover, although 5 years after T_0, there was no re intervention on FC, aortic remodeling was observed at T_1. This prompts us to be cautious about the term "favorable case" and to rather consider this case as a slow evolving case compared to the UFC, a fast evolving case. The choice concerning the open-ended false lumen can also be discussed in the case of FC but in the absence of morphological indications, this choice made it possible to propose a comparison between UFC and FC. Including the aortic valve could have been considered, however both patients have an aortic tricuspid valve without valvular specificity or pathology that can lead to changes in flow shape and their ascending segment were covered by a prosthesis with a constant diameter so that the flow was not disturbed. The interest of including aortic valve was so limited compared to both increase of modeling complexity and computational time that would have been generated. Another limit concerned FSI. It has been shown that rigid wall modeling especially overestimates wall shear stress, and that flap mobility influences hemodynamics in both lumens [7]. None of the few existing FSI studies, however, considers the specific mechanical behavior of aortic walls and flap. RTBAD FSI modeling should provide a better understanding of the disease's evolution mechanisms, for optimized patient prognosis and outcomes. Our team is currently working on results from mechanical characterization of the neointimal flap and aortic dissected wall [17] and patient-specific inlet flow using MRI 4D flow data which were beyond the scope of the present work. As it stands our work used patient-specific geometrical conditions and physiological boundary conditions. Another important advance would be addressing thrombus modeling, to analyze the effects of the false lumen's degree of permeability on the evolution of the pathology.

3.7 Conclusion

The aim of this study was not to make statistics to define new discrimination criteria but to show that it was possible to correlate a biomechanical study with clinical events observed during postoperative follow-up. Our CFD results demonstrate that the morphological features identified and the analysis of hemodynamics performed at T_0 could predict adverse outcomes like thrombus formation, widening of the entry tear section, and false lumen expansion occurring 12 months later. For the first time here, unfavorable evolution is distinguished from favorable development, based on both quantified analysis of hemodynamics at the two follow-ups and CT-angioscan observations on two patients. Given their roles in deleterious clinical events, the flow rate in the false lumen as well as high WSS values jointly analyzed with VS dynamics could be considered biomechanical indicators allowing early (at T_0) evaluation of RTBAD evolution as favorable or unfavorable. Although these comparisons could only be conducted on 2 patients and need to be confirmed by a larger number of cases, this study highlights the relevance of biomechanical simulations in the management of dissections at the earliest stage.

Appendix. Windkessel model implementation

This reduced model describes hydraulic systems through an electrical mechanical analogy where pressure (P) and flow rate (Q) are respectively analogous to voltage and current intensity. This led to the following equation:

$$P(t) + R_2 C \frac{\partial P(t)}{\partial t} = (R_1 + R_2) Q(t) + R_1 R_2 C \frac{\partial Q(t)}{\partial t} \quad (1)$$

with R_1 and R_2 being the proximal and distal resistance, respectively, and C being the capacitance.

The instantaneous pressure at each outlet was then expressed by approximating the derivative terms using the Euler backward scheme, as follows:

$$P_t = \left(\frac{1}{1 + \frac{R_2 C}{dt}} \right) \left[\frac{R_2 C}{dt} P_{t-1} + \left(R_1 + R_2 + \frac{R_1 R_2 C}{dt} \right) Q_t - \frac{R_1 R_2 C}{dt} Q_{t-1} \right]$$

$$(2)$$

The model parameters R_1, R_2 and C for each outlet were identified through an optimization procedure using a genetic algorithm and Matlab software. The optimization problem consisted in finding R_1^i, R_2^i, and C^i for each outlet i that minimize the mismatch between the computed (comp) and the targeted (obj) pressure values. This mismatch M_i is termed the objective function.

$$M_i = \sqrt{(P_{max,comp} - P_{max,obj})^2 + (P_{min,comp} - P_{min,obj})^2 + (P_{mean,comp} - P_{mean,obj})^2} \qquad (3)$$
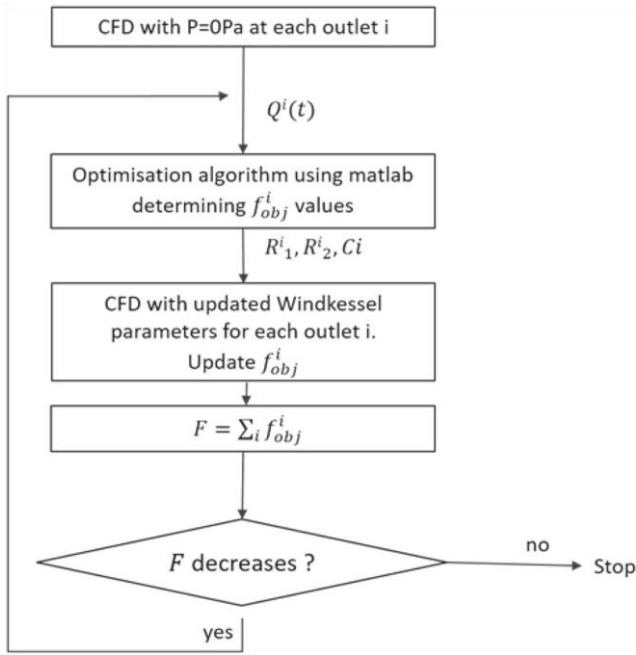
Fig. 9 Windkessel implementation procedure

Pressure values corresponding to the hypotensive therapy prescribed to the patient were targeted to obtain physiological pressure values $P \in [80,120]$ mmHg with $P_{max,obj} =$

120 mmHg, $P_{min,obj}$ = 80 mmHg and $P_{mean,obj}$ = 100 mmHg.

Two constraints were added

1. Pressure curves must be periodic: $P_{t=0} = P_{t=T}$

2. Equation 1 must be verified in the frequency domain when $\omega \to 0$ so $Q^{P\text{-}^-} = R_1 + R_2$.

The global optimization procedure was inspired by the work of [4]. The first estimation of flow rate (shapes and values) was obtained through an independent CFD simulation with zero-pressure at each outlet. This has the merit of providing flow rate curves compatible with the morphology of the patients. These curves were then used for a first estimation of the Windkessel parameters using optimization procedure implemented in Matlab software based on genetic algorithm. The targets (pressure values corresponding to anti-hypertensive treatment) were approximated within a tolerance of 10-^{16}, the optimization result was also evaluated through the Pearson correlation Coefficient r_2 which always exceeded 0.99 for each optimization and each outlet. A new simulation was then carried out with Windkessel models defined at each outlet with the estimated parameters. This helped update the flow rate curves that were used again in the optimization procedure (new CFD simulation plus genetic algorithm) and so on until the convergence condition was met. At the end of a step, the objective function (Eq. 3) was assessed for each outlet using the computed pressure values. Their sum was then compared to its value from the previous iteration. If it decreased (meaning that there was still room for minimizing the difference between the computed values and the targeted values) a new optimization iteration was made, else we stopped the procedure and the last parameters estimated were used for the numerical simulations. This procedure is summed up in Fig. 9.

	BCA/S_1		LCCA/S_2		LS/S_3		DA/S_4	
	Unfavorable case							
	T_0	T_1	T_0	T_1	T_0	T_1	T_0	T_1
R_1 (10^7 $kg.m^{-4}.s^{-1}$)	1.037	1.004	1.064	1.121	1.117	1.176	2.364	2.409
R_2 (10^9 $kg.m^{-4}.s^{-1}$)	1.393	1.394	1.964	2.148	1.911	2.233	0.151	0.146
C (10^{-9} $kg^{-1}.m^4.s^2$)	3.089	4.008	1.835	1.619	2.455	2.026	9.186	8.898
	Favorable case							
	T_0	T_1	T_0	T_1	T_0	T_1	T_0	T_1
R_1 (10^7 $kg.m^{-4}.s^{-1}$)	1.203	0.953	2.82	4.093	1.03	1.76	3.81	2.97
R_2 (10^9 $kg.m^{-4}.s^{-1}$)	0.461	0.597	1.84	2.078	0.993	1.07	0.22	0.198
C (10^{-9} $kg^{-1}.m^4.s^2$)	5.92	4.55	1.29	1.43	2.27	2.75	6.91	6.91

Table 2 Estimated Windkessel parameters

When optimization procedure was ended, that was after several iterations and several CFD simulations, new simulations were carried out, for the current study, with the set of optimal parameters for the Windkessel models at each outlet. Table 2 summarizes the final parameter values of Windkessel model.

Table 3 shows the percentage of flow rate at outlets in relation to inlet one obtained, using Windkessel models at the outlets during simulations. The obtained values are in the range of physiological ones in vivo recorded [6].

	S_1		S_2		S_3		S_4	
	T_0	T_1	T_0	T_1	T_0	T_1	T_0	T_1
UFC	10.13%	9.35%	6.67%	6%	9.35%	7.34%	73.62%	77.46%
FC	27.55%	22.20%	7.51%	6.34%	13.86%	13.52%	51.25%	57.92%
[6]	12.00%		4.05%		4.83%			
[36]	19.01%		5.93%		9.26%			

Table 3 Percentage of flow rate at outlets in relation to inlet one. Mean physiological values recorded from PC-MRI measurements in 4 patients with thoracic aortic diseases [6] and in the TBAD computational model developed by [36] are given for comparison

Declarations

Ethics approval Approval number 2019-48

Competing interests The authors declare no competing interests.

References

1. Ab Naim WN, Ganesan PB, Sun Z, Chee KH, Hashim SA, Lim E (2014) A perspective review on numerical simulations of hemodynamics in aortic dissection. The Scientific World Journal, 652520–12
2. Ab Naim WN, Ganesan PB, Sun Z, Osman K, Lim E (2014) Theimpact of the number of tears in patient-specific stanford type B aortic dissecting anurysm: CFD simulation. J Mech Med Biol 14(2):1450017
3. Ab Naim WN, Ganesan PB, Sun Z, Liew YM, Qian Y, Lee CJ, Jansen S, Hashim SA, Lim E (2016) Prediction of thrombus formation using vortical structures presentation in stanford type b dissectio: a preliminary study using CFD approach. Appl Math Model 40:3115–3127

4. Alimohammadi M, Agu O, Balabani S, Diaz-Zuccarini V (2014) Development of a patient-specific simulation tool to analyse aortic dissections: assessment of mixed patient-specific flow and pressure boundary conditions. Med Eng Phys 36:275–284

5. Alimohammadi M, Pichardo-Almarza C, Agu O, Diaz-ZuccariniV (2016) Development of a patient-specific multi-scale model to understand atherosclerosis and calcification locations: comparison with in vivo data in aortic dissection. Front Physio 7:238

6. van Bakel TM, Romarowski RM, Morganti S, van Herwaarden JA,Moll FL, de Baufort HW, Marrocco-Trishitta MM, Secchi F, Conti M, Auricchio F, Trimarchi S (2018) Blood flow after endovascular repair in the aortic arch: a computational analysis. Aorta 6:81–87

7. Baumler K, Vedula V, Sailer AM, Seo J, Chiu P, Mis-¨ telbauer G, Chan FP, Fischbein MP, Marsden AL, Fleischmann D (2020) Fluid structure interaction simulations of patient specific aortic dissection. Biomech Model Mechan. https://doi.org/10.1007/s10237-020-01294-8

8. Berguer R, Parodi JC, Schlicht M, Khanafer K (2015) Experimental and clinical evidence supporting septectomy in the primary treatment of acute type b thoracic aortic dissection. Ann Vasc Surg 29:167–173

9. Biasetti J, Hussain F, Gasser TC (2011) Blood flow and coherentvortices in the normal and aneurysmatic aortas: a fluid dynamical approach to intra-luminal thrombus formation. J R Soc Interface 8:1449–1461

10. Balabani M, Bonfanti S, Greenwood JP, Puppala S, HomerVanniasinkam S, Diaz-Zuccarini V (2017) Computational tools for clinical support: a multi-scale compliant model for haemodynamic simulations in an aortic dissection based on multi-modal imaging data. J R Soc Interface 14:20170632

11. Carnevale D, Lembo G, Frati G (2011) Chronic Type A aorticdissection: could surgical intervention be guided by molecular markers ? J Cell Mol Med 15(7):1615–1619

12. Chen D, Mu¨ller-Eschner M, Kotelis D, Bockler D, Ventikos Y,¨ von Tengg-Kobligk H (2013) A longitudinal study of type B aortic dissection and endovascular repair scenarios: computational analysis. Med Eng Phys 35:1320–1330

13. Cheng Z, Riga C, Chan J, Hamady M, Wood NB, Cheshire NJ, XuY, Gibbs RGJ (2013) Initial findings and potential applicability of computational simulation of the aorta in acute type b dissection. J Vasc Surg 57:35–43

14. Cheng Z, Kidher E, Jarral OA, O'Regan DP, Wood NB,Athanasiou T, Xu XY (2015) Assessment of hemodynamic conditions in the aorta following root replacement with composite valve-conduit graft. Ann Biomed Eng 44(5):1392–1404

15. Cyron C, Humphrey J (2017) Growth and remodeling of loadbearing biological soft tissues. Adv Biomech: From Found Appl 52:645–664

16. Deplano V, Guivier-Curien C, Bertrand E (2016) 3D analysisof vortical structures in an abdominal aortic aneurysm by stereoscopic PIV. Exp Fluids 57:167

17. Deplano V, Boufi M, Gariboldi V, Loundo AD, D'Journo XB,Cautela J, Djemli A, Alimi Y (2019) Mechanical characterisation of human ascending aorta dissection. J Biomech 94:138–146

18. Doyle BJ, Norman PE (2016) Computational biomechanics inthoracic aortic dissection: today's approaches and tomorrow's opportunities. Ann Biomed Eng 44(1):71–83

19. Ergin MA, Phillips RA, Galla JD, Lansman SL, MendelsonDS, Quintana CS, Griepp RB (1994) Significance of distal false lumen after type a dissection repair. Ann Thorac Surg 57:820– 825

20. Fattori R, Bacchi-Reggiani L, Bertaccini P, Napoli G, Fusco F,Longo M, Pierangeli A, Gavelli G (2000) Evolution of aortic dissection after surgical repair. Am J Cardiol 86:868–872

21. Fattouch K, Sampognaro R, Navarra E, Caruso M, Pisano C,Coppola G, Speziale G, Ruvolo G (2009) Long-term results after repair of type a acute aortic dissection according to false lumen patency. Ann Thorac Surg 88:1244–1250

22. Fung YC (1996) Biomechanics. Circulation. Springer, New York

23. Geirsson A, Bavaria JE, Swarr D, Keane MG, Woo YJ, Szeto WY,Pochettino A (2007) Fate of the residual distal and proximal aorta after acute type a dissection repair using a contemporary surgical reconstruction algorithm. Ann Thorac Surg 84:1955–1964

24. Guzzardi DG, Barker AJ, van Ooij P, Malaisrie SC, PuthumanaJJ, Belke DD, Mewhort HE, Svystonyuk DA, Kang S, Verma S, Collins J, Carr J, Bonow RO, Markl M, Thomas JD, McCarthy PM, Fedak PW (2015) Valve-related hemodynamics mediate human bicuspid aortopathy. J Am Coll Cardiol 66:892– 900

25. Halstead JC, Meier M, Etz C, Spielvogel D, Bodain C, Wurm M,Shahani R, Griepp RB (2007) The fate of the distal aorta after repair of acute type a aortic dissection. J Thorac Cardiov Sur 13:127–135

26. Hellums JD, Peterson DM, Stathopoulos NA, Moake JL, GiorgioTD (1987) Studies on the mechanisms of shear-induced platelet activation. In: Hartmann A, et Kuschinsky W (eds) Cerebral Ischemia and Hemorheology. Springer, Berlin, pp 80–89

27. Khannous F (2020) Modelisation biom´ ecanique et pathologies de´ l'aorte. Suivi clinique dans le contexte de la dissection aortique de type B residuelle. PhD Thesis Aix-Marseille Universit´   e´

28. Leuprecht A, Perktold K (2001) Computer simulation of nonnewtonian effects on blood flow in large arteries. Comput Method Biomech Biomed Eng 4:149–163

29. Lorensen WE, Cline HE (1987) Marching cubes: a high resolution 3d surface construction algorithm. Comp Graph 21:163– 169

30. Lorenzo-Ginori JV, Orozco-Morales R (2013) Cell MicroscopyImaging: A Review on Digital Image Processing Applications. Monograph, Feijoo Ed. ISBN 978-959-250-895-8´

31. Menichini C, Cheng Z, Gibbs RG, Xu XY (2016) Predicting falselumen thrombosis in patient-specific models of aortic dissection. J R Soc Interface 13:20160759–1–11

32. Menichini C, Xu XY (2016) Mathematical modeling of thrombusformation in idealized models of aortic dissection: initial findings and potential applications. J Math Biol 73:1205–1226

33. Menichini C, Cheng Z, Gibbs RG, Xu XY (2018) A computationalmodel for false lumen thrombosis in type b aortic dissection following thoracic endovascular repair. J Biomech 66:36–43

34. Mousavi SJ, Farzaneh S, Avril S (2019) Patient-specific predictions of aneurysm growth and remodeling in the ascending thoracic aorta using homogenized constrained mixture model. Biomech Model Mechanobiol. https://doi.org/10.1007/s10237019-01184-8

35. Olufsen MS, Peskin CS, Kim WY, Pedersen EM, Nadim A,Larsen J (2000) Numerical simulation and experimental validation of blood flow in arteries with structured-tree outflow conditions. Ann Biomed Eng 28:1281–1299

36. Qiao Y, Fan J, Ding Y, Zhu T, Luo K (2020) A primarycomputational fluid dynamics study of pre- and post-TEVAR with intentional left subclavian artery coverage in a type B aortic dissection. J Biomech Eng 141:111002-1

37. Rinaudo A, D'Ancona G, Lee JJ, Pilato G, Amaducci A, BagliniR, Follis F, Pilato M, Salvatore P (2014) Predicting outcome of aortic dissection with patent false lumen by computational flow analysis. Cardiovasc Eng Techn 5(2):176–188

38. Ruggeri ZM, Mendolicchio GL (2007) Adhesion mechanism inplatelet function. Circ Res 100:1673–1685

39. Shang EK, Nathan DP, Fairman RM, Bavaria JE, Gorman RC,Gorman IIIJH, Jackson BM (2015) Use of computational fluid dynamics studies in predicting aneurysmal degeneration of acute type b aortic dissections. J Vasc Surg 62:279–284

40. Song S-W, Chang B-C, Cho B-K, Yi G, Youn Y-N, Lee S, Yoo KJ (2010) Effects of partial thrombosis on distal aorta after repair of acute debakey type i aortic dissection. The J Thorac Cardiovasc Surg 139:841–847

41. Tsai M-T, Wu H-Y, Roan J-N, Tsai Y-S, Hsieh PC, Yang YJ, Luo C-Y (2014) Effect of false lumen partial thrombosis on repaired acute type a aortic dissection. J Thorac Cardiovasc Surg 148:2140–2146

42. Tse KM, Chiu P, Lee HP, Ho P (2011) Investigation ofhemodynamics in the development of dissecting aneurysm within patient-specific dissecting aneurismal aortas using computational fluid dynamics (CFD) simulations. J Biomech 44:827–836

43. Xu H, Piccinelli M, Leshnower BG, Lefieux A, Taylor WR,Veneziani A (2018) Coupled morphological hemodynamic computational analysis of type b aortic dissection: a longitudinal study. Ann Biomed Eng 46:927–939

44. Zierer A, Voeller RK, Hill KE, Kouchoukos NT, Damiano RJ,Moon MR (2007) Aortic enlargement and late reoperation after repair of acute type a aortic dissection. Ann Thorac Surg 84:479– 487

45. Zhou J, Adrian RJ, Balachandar S, Kendall TM (1999) Mechanisms for generating coherent packets of hairpin vortices in channel flow. J Fluid Mech 387:353–396